Design methodology for porous composites with tunable thermal expansion produced by multi-material topology optimization and additive manufacturing

Akihiro Takezawa[a,*], Makoto Kobashi[b]

[a]*Department of Transportation and Environmental Systems, Graduate school of Engineering, Hiroshima University, 1-4-1 Kagamiyama, Higashi-Hiroshima, Hiroshima 739-8527, Japan*

[b]*Department of Materials Process Engineering, Graduate School of Engineering, Nagoya University, Furo-cho, Chikusa-ku, Nagoya 464-8603, Japan*

Abstract

To realize negative thermal expansion (NTE), porous composites made of two materials with different coefficients of thermal expansion are being actively researched. NTE can be realized by taking advantage of the thermal deformation mechanisms of a composite material's internal geometry. However, in addition to negative thermal expansion, materials with anisotropic and large positive thermal expansion are also desirable for various applications. Also, additive manufacturing provides new ways to fabricate composites by layering multiple materials at arbitrary points in three-dimensional space. In this study, we developed a design methodology for porous composites, which showed defined thermal expansion characteristics, including negative and positive thermal expansion as well as isotropic and anisotropic thermal expansion. Our approach was tested based on the fabrication of a

*Corresponding author. Tel: +81-82-424-7544; Fax: +81-82-422-7194

Email addresses: akihiro@hiroshima-u.ac.jp (Akihiro Takezawa), kobashi@numse.nagoya-u.ac.jp (Makoto Kobashi)

multi-material photopolymer by additive manufacturing. The internal geometries required to produce such characteristics were designed by topology optimization, which is the most effective structural optimization method for realizing macroscopic inward deformation and for maintaining stiffness. The designed structures were converted to three-dimensional models and fabricated by multi-material photopolymer additive manufacturing. Using laser scanning dilatometry, we measured the thermal expansion of these specimens, revealing well-ordered thermal expansion, from anisotropic positive thermal expansion to anisotropic negative thermal expansion, over a wide range of about $-3 \times 10^{-4}\mathrm{K}^{-1}$ to $1 \times 10^{-3}\mathrm{K}^{-1}$.
Keywords: Polymer-matrix composites (PMCs), Thermomechanical, Computational modelling, Finite element analysis (FEA), Additive manufacturing

1. Introduction

Thermal expansion is an important phenomenon in many applications. A large positive thermal expansion (PTE) is useful in thermal actuators and medical vessel dilators that operate based on human body temperature. A negative thermal expansion (NTE) is useful for canceling the thermal expansion of ordinary materials in high-temperature or high-precision devices. Because naturally occurring NTE is rare, materials that exhibit NTE have drawn considerable attention (e.g. [1, 2, 3]). However, NTE is limited to specific perovskite ceramics and tuning of NTE performance remains challenging.

Another way to realize NTE is by constructing a porous composite of

two materials with different coefficients of thermal expansion (CTE). This approach can realize an effective (macroscopic average) NTE because of the internal geometry of the composite. For example, as the temperature rises, the system may exhibit inward deformation toward voids in the internal geometry, induced by bending of layers of materials that show different thermal expansion such as bimetals. Both theoretical and experimental studies of materials with negative thermal expansion and their internal structures, have been performed [4, 5, 6, 7, 8, 9, 10, 11, 12, 13].

The design of the internal structure of porous composites, which allow for inward deformation, must consider the thermal deformation of the composite materials, which is related to their stiffness and CTE. Numerical structural optimization could be a powerful way to design complicated structures, because it allows for automatic structural optimization through numerical structural analysis and optimization techniques. In particular, topology optimization can be used to fundamentally optimize the target structure, including the number of void spaces[14]. This approach could be used in the design of composite materials and structures [4, 11, 12, 15]. Some studies have used topology optimization to tune the negative thermal expansion of materials based on their internal geometry [4, 11, 12]. Although these approaches can generate structures that match arbitrary performance targets, the study of CTE topology optimization has been limited to isotropic NTE behavior. However, devices that require only axial NTE or an extra-large PTE might also have valuable applications.

On the experimental side, additive manufacturing and rapid prototyping have been used [16] to produce detailed 3D structures. Recent developments

in technology have improved the manufacturing accuracy and the level of detail possible in 3D composites and porous materials to a scale of about 10μm. Such small-scale fabrication can be used to develop novel composite materials [15, 17, 18, 19, 20, 21]. Additive manufacturing could be another approach that can easily produce multi-material composites by controlling the location of the supplied material. This is a simpler process for the fabrication of NTE porous composites, which usually requires involved techniques such as micro-fabrication by co-extrusion and reduction sintering [6] or microelectromechanical fabrication [10]. Thus, additive manufacturing could be an effective way to simply fabricate porous composites that show NTE behavior [12, 13].

In the present study, we developed a design methodology for porous composites with arbitrary thermal-expansion characteristics derived from their internal geometry. For the first time we also examined NTE together with isotropic and anisotropic, extra-large effective PTE behaviors in these structures. We used a numerical topology optimization based on the finite element method (FEM), to design the internal geometry and maximize the macroscopic inward or outward deformation while maintaining a certain stiffness. Test pieces with the designed internal structure were fabricated from a photopolymer by additive manufacturing. The internal thermal expansion of the test pieces was verified by measuring their thermal deformation with a laser scanning dilatometer.

2. Theoretical background of design methodology

2.1. Mechanics of porous composites

Here, we investigate the thermal expansion of a porous composite having an internal structure with a periodic layout in a plane using FEM. We assume that the thermal expansion of the material's internal structure follows linear elastic theory:

$$\sigma_{ij} = C_{ijkl}(\epsilon_{kl} - \Delta T \alpha_{kl}) = C_{ijkl}\beta_{kl}, \tag{1}$$

where $\boldsymbol{\sigma}$, $\mathbf{C}$, $\boldsymbol{\epsilon}$, $\boldsymbol{\alpha}$, and $\boldsymbol{\beta}$ are the stress tensor, elastic tensor, strain tensor, CTE tensor, and thermal stress tensor, and ΔT is the temperature change from a reference temperature. The displacement $\mathbf{u}$ is related to the strain by $\boldsymbol{\epsilon} = \frac{1}{2}\left\{\nabla\mathbf{u} + (\nabla\mathbf{u})^{\mathrm{T}}\right\}$. By solving this equation though FEM, after setting appropriate boundary conditions, one can determine the displacement distribution of the internal geometry of the porous composite caused by thermal expansion.

The effective physical properties of a porous material with a repeating unit cell can be calculated by numerical homogenization [22, 23, 24]. The effective elastic tensor $\mathbf{C}^H$, CTE tensor $\boldsymbol{\alpha}^H$, and thermal stress tensor $\boldsymbol{\beta}^H$ of the periodic structure composed of a unit cell Y are calculated as:

$$C^H_{ijkl} = \frac{1}{|Y|}\int_Y \left(C_{ijkl} - C_{ijpq}\frac{\partial \chi^{kl}_p}{\partial y_q}\right) \mathrm{d}Y, \tag{2}$$

$$\alpha^H_{ij} = [C^H_{ijkl}]^{-1}\beta^H_{pq} = [C^H_{ijkl}]^{-1}\frac{1}{|Y|}\int_Y \left(\beta_{pq} - C_{pqkl}\frac{\partial \psi_k}{\partial y_l}\right) \mathrm{d}Y, \tag{3}$$

where $\boldsymbol{\chi}$ and $\boldsymbol{\psi}$ are the values of displacement obtained by solving the prob-

lem of Y-periodic cells expressed as:

$$\int_Y C_{ijpq}\left(\delta_{pk}\delta_{ql} - \frac{\partial \chi_p^{kl}}{\partial y_q}\right)\frac{\partial v_i}{\partial y_j}\mathrm{d}Y = 0, \tag{4}$$

$$\int_Y \left(\beta_{ij} - C_{ijkl}\frac{\partial \psi_k}{\partial y_l}\right)\frac{\partial v_i}{\partial y_j}\mathrm{d}Y = 0, \tag{5}$$

where $\mathbf{v}$ is an arbitrary test function. As for Eq. (1), these equations are solved by FEM.

2.2. Optimization methodology

The internal geometry of the porous composite was designed by optimizing its thermal deformation. We set the unit base shape of the internal geometry to be a square domain and allocated two types of photopolymers and void space. We designed the internal geometry of the solid isotropic material with penalization (SIMP)-based multiphase topology optimization [4, 25]. The approach lays out the three phases, i.e., the two materials and void space, in the specified domain by defining two artificial density functions ϕ_1 and ϕ_2 $(0 < \phi_1, \phi_2 \leq 1)$ on a fixed design domain. The elastic modulus and CTE were formulated as functions of ϕ_1 and ϕ_2, which represent the existence of the materials and their type, respectively, to physically relate these functions to the target optimization. Hence the local Young's modulus and CTE of the designed target domain are represented as:

$$E(\phi_1, \phi_2) = \phi_1^3\left\{\phi_2 E_1 + (1-\phi_2)E_2\right\}, \tag{6}$$

$$\alpha(\phi_2) = \phi_2\alpha_1 + (1-\phi_2)\alpha_2, \tag{7}$$

where E_1, E_2, α_1, and α_2 are the Young's modulus and CTE of photopolymers 1 and 2, respectively. In other words, after updating the functions ϕ_1 and ϕ_2

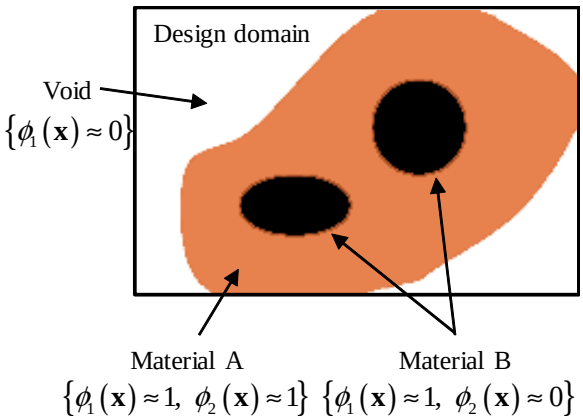

Figure 1: Outline of the domain representation by multi-material topology optimization.

with an optimization algorithm, the resulting values of $\phi_1 \approx 1$ and $\phi_2 \approx 1$ indicate the existence of photopolymer 1, $\phi_1 \approx 1$ and $\phi_2 \approx 0$ indicate the existence of photopolymer 2, and $\phi_1 \approx 0$ indicates the existence of a void at a position $\mathbf{x}$ in the fixed design domain, as shown in Fig. 1. These values are set to be either 0 or 1 in the optimization settings, as intermediate values are not resulted.

We optimized the effective CTE using the displacement of the internal geometry obtained by solving Eq.(1) in the objective function. A typical choice of objective function in CTE design is the effective thermal stress tensor [4, 12] instead of the effective CTE. The effective CTE itself is not suitable as an objective function because it contains the inverse of the effective stiffness tensor and produces geometry with insufficient stiffness. However, in a few cases, a structure with a negative effective stress tensor does not exhibit inward deformation during optimization, because the effective stress tensor represents the average stress of the internal geometry. Thus, we introduced the displacement of the connected parts of the internal geometry as a more

direct objective function used to realize inward or outward deformation.

Topology optimization that considers only the deformation of the internal geometry could produce a structure with very low stiffness, which would be unsuitable for fabrication and experiments. We thus intended to maintain a certain effective stiffness while maximizing the inward or outward deformation by setting the multi-objective function as:

$$\underset{\phi_1,\phi_2}{\text{minimize}}\, J(\phi_1,\phi_2) = -w * C^H_{iiii} + (1-w) * \int_{\Omega_{\text{def}}} a_i u_i \mathrm{d}x \ (i=1,2), \qquad (8)$$

where **a** is a vector deciding the sign and component of the displacement used in the objective function.

A flowchart of the optimization procedure is shown in Fig. 2. We first calculated the effective physical properties and the objective function in Eq. (8), using FEM. Because the density function was updated by gradient-based algorithms, the first-order gradient of the objective function was then calculated using the adjoint method [26]. The density functions ϕ_1 and ϕ_2 were updated by the method of moving asymptotes (MMA) [27] during the first optimization stage. In the second stage, to obtain a clear shape that avoided intermediate values, the density function was updated using the phase field method [28].

3. Design of internal geometry

3.1. Materials

On the basis of the numerical design methodology described above, we designed the internal geometry of the photopolymer composite. The test pieces

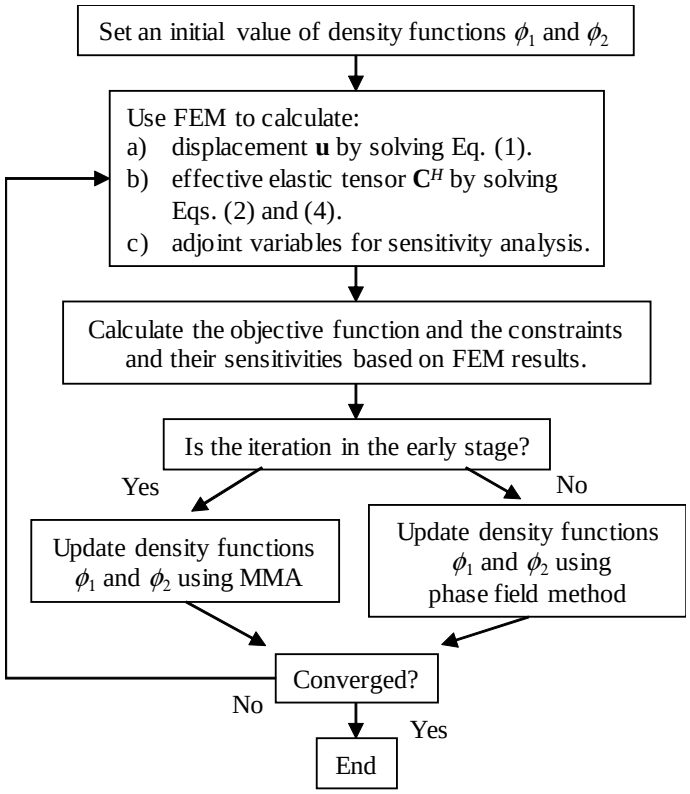

Figure 2: Flowchart of the topology optimization procedure.

were fabricated with an Objet Connex 500 (Stratasys Ltd., USA), a commercial photopolymerization machine capable of multi-material 3D printing with a build resolution $600 \times 600 \times 1600$ dpi (xyz), 0.016 mm layer thickness and approximately 0.05-mm shape accuracy. The machine produced 3D structures through ink-jet printing, which involved spraying a liquid photopolymer onto a build tray in thin layers, which were then exposed to ultraviolet light to solidify the photopolymer. By depositing different materials at locations defined by the optimized design, we fabricated multi-material composites. When producing structures from multiple materials, a rigid material, such a rubber-like material, and several admixtures of materials can be used. Figure 3 shows a simple model fabricated from two materials indicated by their black and white color. The interface of the materials was approximately 0.5 mm thick formed from a graded mixture of the two materials to ensure a strong connection. The fabrication of the functional part was achieved by combining the two materials in small dots to achieve a mixing state, similar to color mixing in the paper inkjet printing. Following our previous work [12], we used VeroWhitePlus RGD835 and FLX9895-DM, which is an admixture of VeroWhitePlus and TangoBlackPlus [29], because this combination could produce the desired stiffness and CTE difference in the temperature range of room temperature to 40 °C. Table 1 lists the relevant CTEs and Young's moduli. To produce a negative effective CTE at 40 °C, i.e., the temperature corresponding to the maximum CTE difference between the materials, we set the Young's modulus and CTE used in the optimization based on the average measured physical properties:

$$E_1 = 290\text{MPa},\ E_2 = 5.0\text{MPa}, \alpha_1 = 1.0 \times 10^{-4}\text{K}^{-1} \text{ and } \alpha_2 = 1.2 \times 10^{-4}\text{K}^{-1}. \tag{9}$$

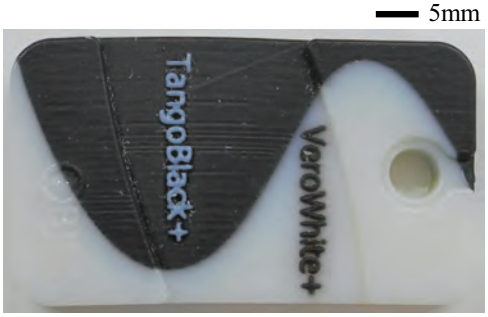

Figure 3: Example of an object fabricated from black and white materials by multi-material photopolymer additive manufacturing device.

Table 1: Measured Young's modulus and CTE of the VeroWhitePlus RGD835 and FLX9895-DM photopolymers. $n = 3$ for each temperature [12].

	VeroWhitePlus RGD835		FLX9895-DM	
Temperature (°C)	Young's modulus (MPa)	CTE ($\times 10^{-5}\text{K}^{-1}$)	Young's modulus (MPa)	CTE ($\times 10^{-5}\text{K}^{-1}$)
20	1996.2 ± 111.2	-	67.8 ± 2.4	-
30	1023.3 ± 228.0	7.14 ± 0.85	13.0 ± 5.4	8.00 ± 1.64
40	288.5 ± 34.6	8.96 ± 1.56	3.8 ± 0.8	10.53 ± 3.10

3.2. Topology optimization

We considered three design cases: case 1, anisotropic NTE (ANTE); case 2, isotropic extra-large positive thermal expansion (IPTE); case 3, anisotropic extra-large PTE (APTE). We expected the order of the axial CTEs to be APTE>IPTE>bulk materials>INTE[12]>ANTE.

Figure 4 shows the design domain. The basic shape of the designed internal geometry is defined as a unit square. The domains evaluating the displacement are defined as the center of the boundaries. For the anisotropic design, only the side domains are activated. For the isotropic design, both the upper and lower domains are activated.

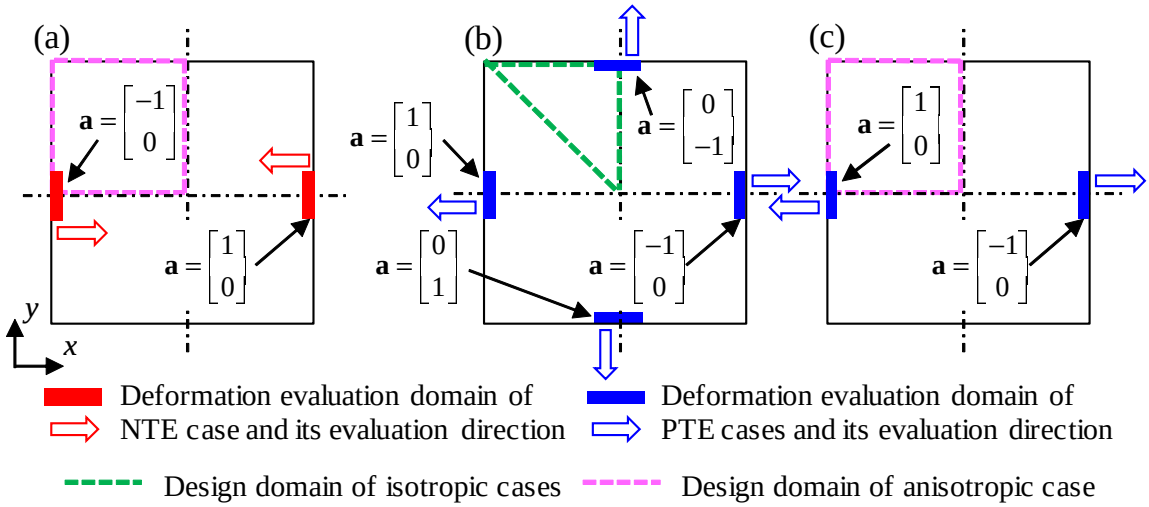

Figure 4: Design domain of each design case. (a) ANTE case, (b) IPTE case, (c) APTE case. The size of the blue and red displacement evaluation domains is 0.2×0.01. In other domains, $\mathbf{a} = \mathbf{0}$.

For the isotropic design, symmetry is assumed along the center and diagonal lines of the square design domain. For the anisotropic design, symmetry is assumed on the centerlines. Thus, distributions of ϕ_1 and ϕ_2 are optimized only on the 1/8 domain in the isotropic case and the 1/4 domain in the anisotropic case, as shown in Fig. 4. These symmetries in the internal geometries are not fundamentally required when designing effective CTEs. Rather, we introduced the symmetry to simplify the optimal geometry, make

fabrication easier, and narrow the design space to effectively search for an optimal solution. We also introduced a forced void domain (marked by gray dots), in which no material can exist, to maintain sufficient space for thermal deformation.

We performed the topology optimization using random distributions of ϕ_1 and ϕ_2 as the initial shapes. All FEM calculations during optimization were performed with the commercial software COMSOL Multiphysics. The first 200 iterations of MMA were based on a 60×60 mesh for the finite element analysis and discretization of ϕ_1 and ϕ_2. We performed another 100 MMA and 100 phase field method optimizations based on a 120×120 mesh for some cases. Figure 5 (d,g,j) shows the final converged solution for each case. For comparison, this figure also shows the isotropic NTE (INTE) structure derived in [12]. We then obtained 3D data in STL format by extruding the two-dimensional (2D) optimal shape in the thickness direction. The 2D views of the STL models are shown in Fig. 5 (e,h,k). The hinge-like parts, which could not likely be fabricated, were replaced by thicker soft photopolymer and isolated parts were removed. The free thermal deformation shapes of these models are shown in Fig. 5 (f,i,h).

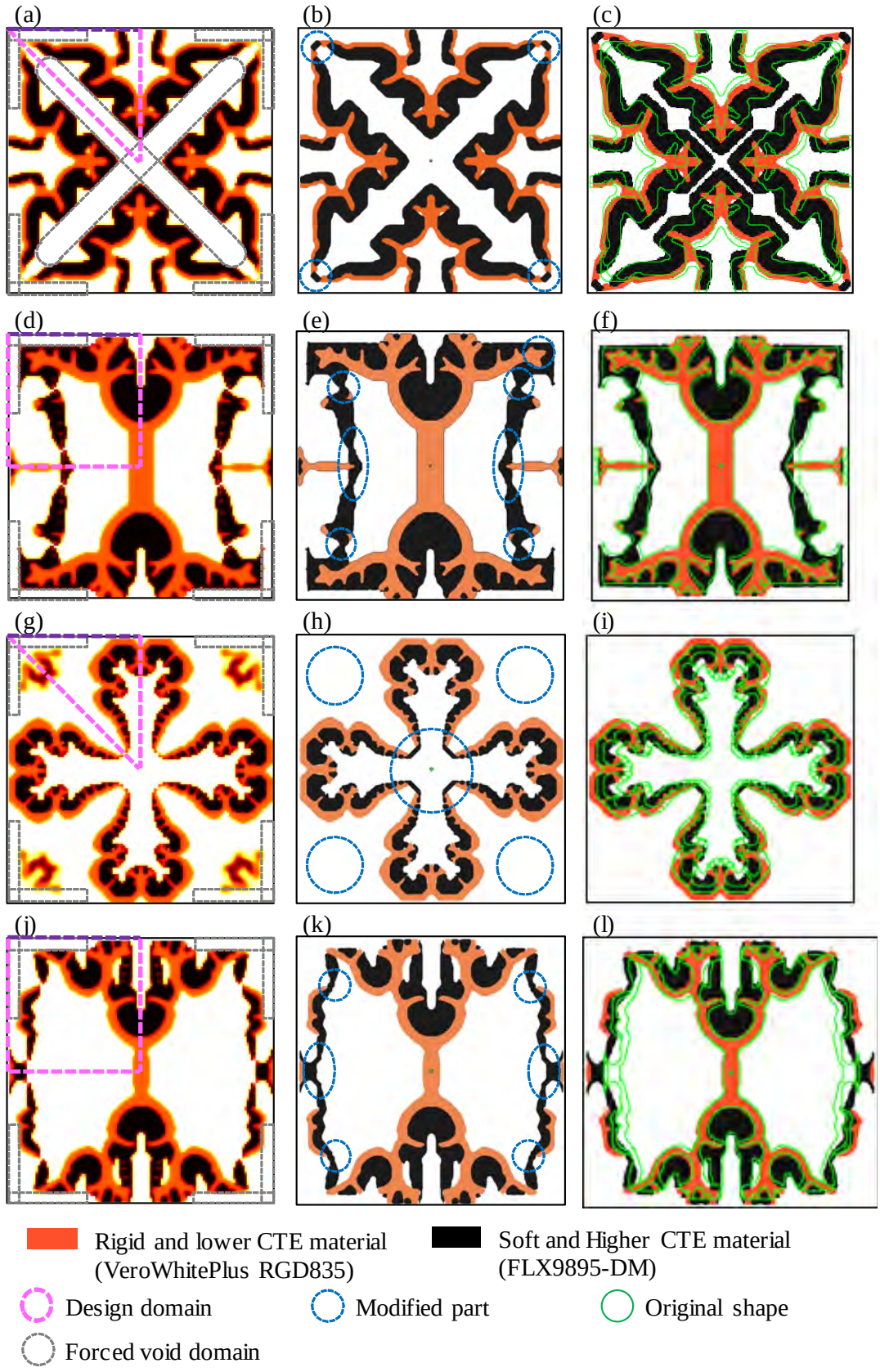

Figure 5: Optimal configurations and 2D views of the STL models. (a), (d), (g), (j): Original results of topology optimization. Pink dotted lines indicate the optimized domains. Gray dotted lines indicate the forced void domain used to maintain the deformation range. (b), (e), (h), (k): 2D views of the STL models generated from the topology optimization. Blue dotted circles indicate the modified parts. (c),(f),(i),(l): Thermal deformation shapes obtained from reanalyzing the STL models. Green lines indicate the original shape. (a)–(c): INTE case [12]. (d)–(f): ANTE case. (g)–(i): IPTE case. (j)–(l): IPTE case.

The main driving force for inward and outward deformation is the bending deformation of a bilayer whose materials have different CTEs. Because the two materials have different CTEs, a bilayer shows bending deformation similar to that of bimetals. These parts are connected by rigid and hinge-like joints. The rigid joints transfer the bending moments to other parts of the structure. The hinge joints help to enlarge the bending deformation, acting as linkages. This kind of deformation mechanism could be discussed in the context of a compliant mechanism [30, 31]. Figure 6 shows a diagram of each mechanism featuring bending and rigid bars as well as rigid and hinge joints. The two anisotropic mechanisms are basically identical, with the top and bottom parts generating compression on both sides and a linkage moving inward or outward. The direction of movement is decided only by the initial angle of the side parts. The inward and outward angles correspond to motion in the same direction.

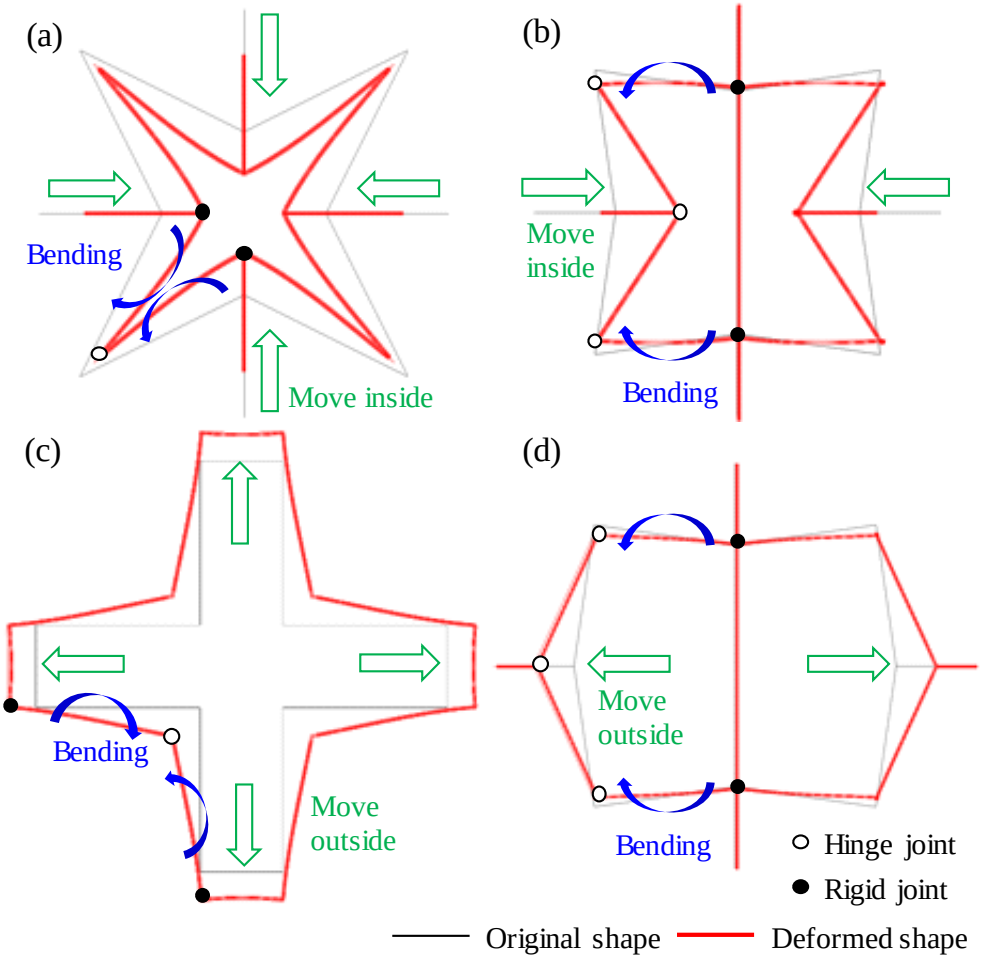

Figure 6: Diagrams showing the mechanisms of the optimal composites. (a) INTE mechanism, (b) ANTE mechanism, (c) IPTE mechanism, (d) APTE mechanism.

Table 2 shows the effective planar mechanical properties of each optimal structure obtained with the homogenization method, based on finite element analysis, on the STL models, with the material properties shown in Eq. (9). The x-directional CTE matched well with the expected order of APTE>IPTE>bulk materials>INTE[12]>ANTE. The anisotropic cases

performed better because of their broader acceptable design space. The anisotropic case must consider only horizontal deformation, while the isotropic cases must consider both horizontal and vertical deformations. The anisotropic case can use a larger bilayer structure, to generate greater bending deformation. However, all of these structures have a common drawback: low stiffness owing to their hinge-like joints.

Table 2: Summary of effective CTE and stiffness of the test pieces, obtained by the homogenization method.

	Effective CTE(K^{-1})		Effective stiffness tensor (MPa)			
Cases	α_{11}^H	α_{22}^H	C_{1111}^H	C_{1122}^H	C_{2222}^H	C_{1212}^H
INTE[12]	-3.53×10^{-5}	-3.53×10^{-5}	4.12×10^{-2}	-1.01×10^{-2}	4.12×10^{-2}	1.90×10^{-3}
ANTE	-1.37×10^{-4}	9.70×10^{-5}	1.53×10^{-2}	-6.88×10^{-2}	12.23	4.35×10^{-3}
IPTE	2.68×10^{-4}	2.68×10^{-4}	4.50×10^{-2}	-9.58×10^{-2}	4.50×10^{-2}	2.93×10^{-4}
APTE	4.35×10^{-4}	9.67×10^{-5}	7.07×10^{-3}	4.66×10^{-2}	8.98	1.68×10^{-2}

4. Experiment

4.1. Fabrication of test pieces

We measured the thermal deformation using laser scanning, which is suitable even for relatively large specimens. The laser scanner was an SL-1600A (Shinagawa Refractories Co., Ltd.), which measures the axial thermal deformation of rod-shaped specimens.

By arranging the eight base STLs, as shown in Fig. 5, in two lines, we constructed the STL model of the test piece. The dimensions of each internal structure were $10 \times 10 \times 10$mm, and the total dimensions of the test piece were $40 \times 20 \times 10$mm. Figure 7 shows an outline and close-up pictures of a

fabricated test piece for each case. A close-up picture of the internal geometry shows that we produced a shape similar to the original STL model, including two key parts: the bi-material layer and the hinge joints.

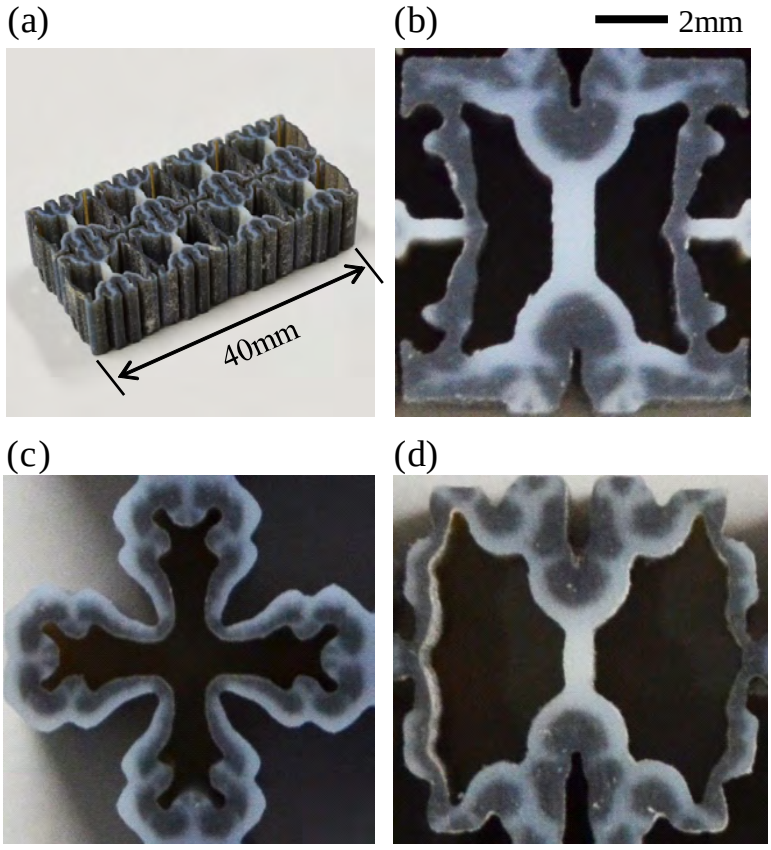

Figure 7: Picture of a test piece. (a) Outline view. (b–d) Close-up view corresponding to the ANTE, IPTE, and APTE cases.

4.2. Measurement of CTE

The thermal expansion of the long sides of test pieces was measured for $n = 3$ samples in the temperature range of room temperature to 50 °C, at a heating rate of 1 °C/min. Figure 8 shows the measured strains for the

ANTE, IPTE, and APTE cases. Initially the thermal expansion showed a linear relationship with temperature and the corresponding CTEs were calculated from the gradient of the approximately straight lines. However, the linear region of each case was small because of the unstable physical properties of the original materials, as described in a previous study [12]. Beyond the linear region, the proposed design framework is not applicable and further experimental studies are required to characterize the behavior. Figure 9 summarizes the approximated CTE values in order together with the analysis results of the CTE shown in Table 2. The CTE values followed the order APTE>IPTE>bulk materials>INTE[12]>ANTE, from both our analysis and experiments, as we predicted. However, there were some large differences between the analysis and experimental results. Moreover, the performance of the fabricated porous material varied widely. These effects might be caused by the very low stiffness of the test pieces and the unstable properties of the bulk materials, as shown in Table 1. Consequently, our results show that although some issues have to be addressed our proposed design framework can be used for quantitative design of the thermal expansion of porous photopolymer composites.

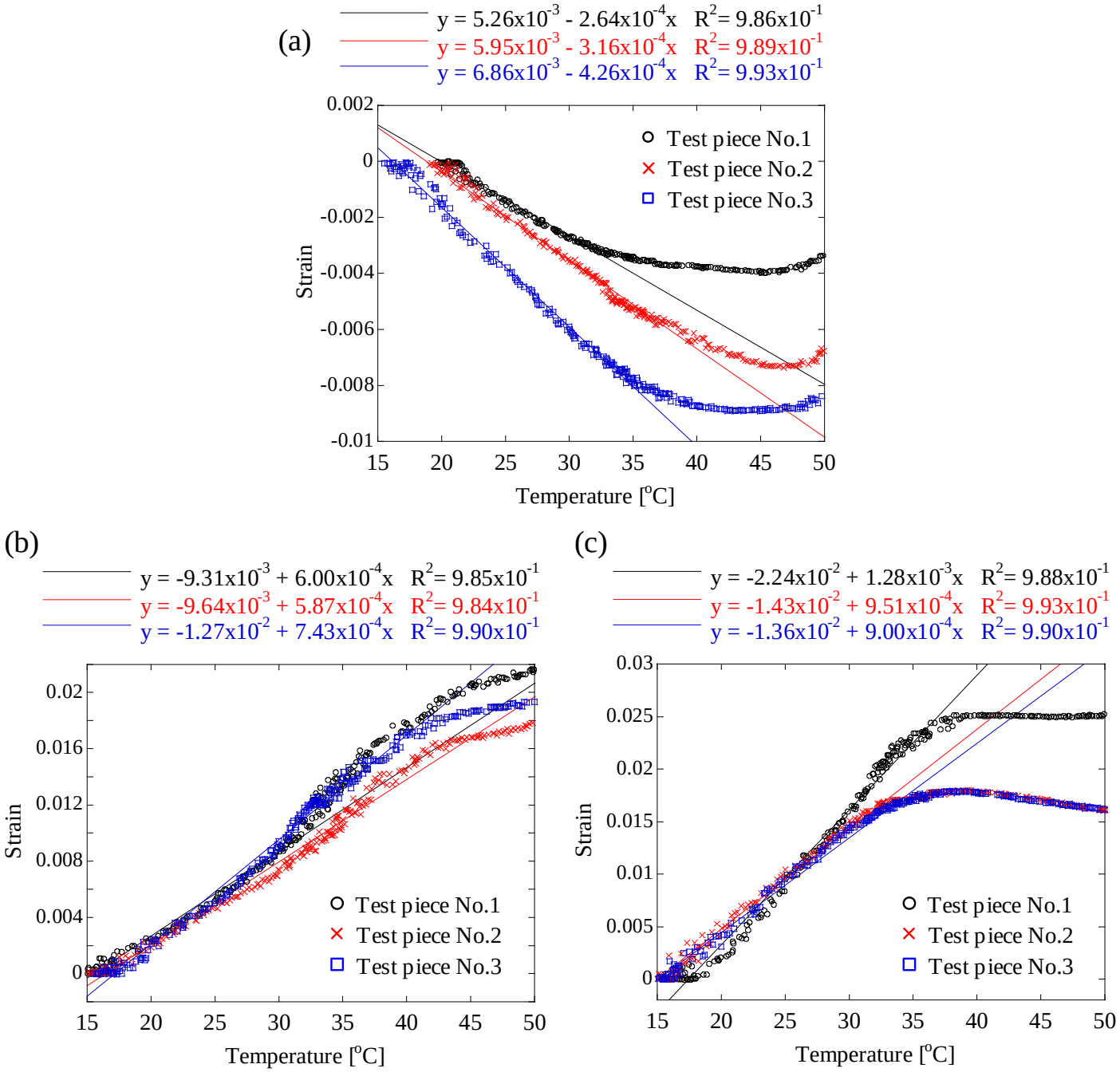

Figure 8: Axial strain of test pieces measured by laser scanning dilatometry. (a) ANTE case, (b) IPTE case, (c) APTE case. Three test pieces were fabricated for each case and the thermal expansion measured once for each. Data from the three measurements are shown in each case. The heating rate was 1 °C/min. The temperature range was room temperature to 50 °C.

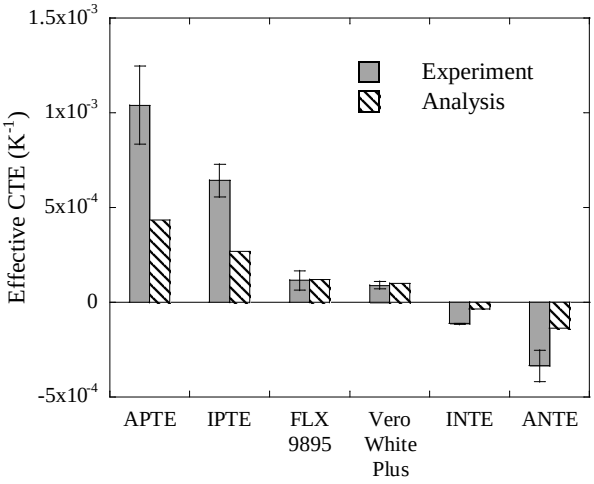

Figure 9: Measured effective CTEs in each case. APTE case: $(1.04 \pm 0.21) \times 10^{-3}\mathrm{K}^{-1}$. IPTE case: $(6.43 \pm 0.87) \times 10^{-4}$ K^{-1}. INTE case [12]: $(-1.14 \pm 0.03) \times 10^{-4}$ K^{-1}. ANTE case: $(-3.35 \pm 0.83) \times 10^{-4}$ K^{-1}. Analysis results shown in Table 2 are also plotted for comparison.

5. Conclusion

Using multi-material topology optimization and photopolymer additive manufacturing, we developed a design methodology for porous composites with arbitrary thermal expansion and studied cases of anisotropic NTE, isotropic PTE, and anisotropic PTE. The validity of the methodology was confirmed by experimental testing. The mechanism allowing arbitrary effective thermal expansion derives from a bi-layer bending component and rigid and hinge-like joints. The optimal 2D internal geometries were converted to STL models, which were then fabricated as test pieces. The thermal expansion of the samples was measured with laser scanning dilatometry. The measured effective CTE values varied in the order APTE>IPTE>bulk materials>0>INTE[12]>ANTE. The anisotropic materials had higher PTE

and NTE because they could make use of a larger space than that of the isotropic material. The minimum and maximum effective CTEs were about $-3 \times 10^{-4}\mathrm{K}^{-1}$ and $1 \times 10^{3}\mathrm{K}^{-1}$, respectively. Hence, we designed materials showing CTE with a wide range of values, -300% to 1000% of the original bulk materials.

However, direct application of these composites remains difficult owing to some drawbacks. First, the materials feature unstable temperature-dependent physical properties. We could not precisely control the effective CTE in this work. This difficulty arises from the strongly temperature-dependent and variable physical properties of the photopolymer. To understand the temperature dependent phenomena of the composites more detailed experiment are required, such as tracking thermal deformation with a camera and image processing. The second drawback is the very low stiffness caused by the hinge-like part of the internal structure and the low stiffness of the rubber like material. These issues may be solved though metal additive manufacturing with multi-material fabrication function such as direct energy deposition [32, 33] and ultrasonic consolidation [34, 35]. The designs obtained in this research are not directly applicable to different materials. However, our proposed methodology can generate alternative appropriate optimal geometries depending on the orbital material properties settings. The use of two kinds of metals having different CTEs with little temperature dependence would likely allow for more exact design of the effective CTE, including a zero CTE, over in wider temperature range, while maintaining the stiffness of the composite.

Acknowledgments

We wish to thank T. Kaneyoshi at the Hyogo Prefectural Institute of Technology and A. Terayama at the Hiroshima Prefectural Technology Research Institute for their technical assistance in experiments. This work was supported by JSPS KAKENHI grant number 15K12557.

References

[1] G. D. Barrera, J. A. O. Bruno, T. H. K. Barron, N. L. Allan, Negative thermal expansion, J. Phys. Condens. Matter 17 (4) (2005) R217.

[2] K. Takenaka, Negative thermal expansion materials: technological key for control of thermal expansion, Sci. Tech. Adv. Mater. 13 (1) (2012) 013001.

[3] K. Takenaka, Y. Okamoto, T. Shinoda, N. Katayama, Y. Sakai, Colossal negative thermal expansion in reduced layered ruthenate, Nat. Comm. 8 (2017) 14102.

[4] O. Sigmund, S. Torquato, Composites with extremal thermal expansion coefficients, Appl. Phys. Lett. 69 (21) (1996) 3203–3205.

[5] R. Lakes, Cellular solid structures with unbounded thermal expansion, J. Mater. Sci. Lett. 15 (6) (1996) 475–477.

[6] J. Qi, J. W. Halloran, Negative thermal expansion artificial material from iron-nickel alloys by oxide co-extrusion with reductive sintering, J. Mater. Sci. 39 (13) (2004) 4113–4118.

[7] J. N. Grima, P. S. Farrugia, R. Gatt, V. Zammit, A system with adjustable positive or negative thermal expansion, in: Proc. Roy. Soc. Lond. Math. Phys. Sci., Vol. 463, 2007, pp. 1585–1596.

[8] R. Lakes, Cellular solids with tunable positive or negative thermal expansion of unbounded magnitude, Appl. Phys. Lett. 90 (22) (2007) 221905.

[9] C. A. Steeves, S. L. S. Lucato, M. He, E. Antinucci, J. W. Hutchinson, A. G. Evans, Concepts for structurally robust materials that combine low thermal expansion with high stiffness, J. Mech. Phys. Solid. 55 (9) (2007) 1803–1822.

[10] N. Yamamoto, E. Gdoutos, R. Toda, V. White, H. Manohara, C. Daraio, Thin films with ultra-low thermal expansion, Adv. Mater. 26 (19) (2014) 3076–3080.

[11] M. Hirota, Y. Kanno, Optimal design of periodic frame structures with negative thermal expansion via mixed integer programming, Optimi. Eng. 16 (4) (2015) 767–809.

[12] A. Takezawa, M. Kobashi, M. Kitamura, Porous composite with negative thermal expansion obtained by photopolymer additive manufacturing, APL Mater. 3 (7) (2015) 076103.

[13] Q. Wang, J. A. Jackson, Q. Ge, J. B. Hopkins, C. M. Spadaccini, N. X. Fang, Lightweight mechanical metamaterials with tunable negative thermal expansion, Phys. Rev. Lett. 117 (17) (2016) 175901.

[14] M. P. Bendsøe, O. Sigmund, Topology Optimization: Theory, Methods, and Applications, Springer-Verlag, Berlin, 2003.

[15] Q. Yang, S. Meng, W. Xie, H. Jin, C. Xu, S. Du, Effective mitigation of the thermal short and expansion mismatch effects of an integrated thermal protection system through topology optimization, Compos. B. Eng. 118 (2017) 149–157.

[16] I. Gibson, D. Rosen, B. Stucker, Additive manufacturing technologies, Springer, 2010.

[17] H. Zhan, F. Cheng, Y. Chen, K. W. Wong, J. Mei, D. Hui, W. M. Lau, Y. Liu, Transfer printing for preparing nanostructured pdms film as flexible sers active substrate, Compos. B. Eng. 84 (2016) 222–227.

[18] X. Wang, M. Jiang, Z. Zhou, J. Gou, D. Hui, 3d printing of polymer matrix composites: A review and prospective, Compos. B. Eng. 110 (2017) 442–458.

[19] P. Tran, T. D. Ngo, A. Ghazlan, D. Hui, Bimaterial 3d printing and numerical analysis of bio-inspired composite structures under in-plane and transverse loadings, Compos. B. Eng. 108 (2017) 210–223.

[20] F. Naddeo, A. Naddeo, N. Cappetti, Novel "load adaptive algorithm based" procedure for 3d printing of lattice-based components showing parametric curved micro-beams, Compos. B. Eng. 115 (2016) 51–59.

[21] Z. Zhang, B. Wang, D. Hui, J. Qiu, S. Wang, 3d bioprinting of soft materials-based regenerative vascular structures and tissues, Compos. B. Eng. 123 (2017) 279–291.

[22] J. M. Guedes, N. Kikuchi, Preprocessing and postprocessing for materials based on the homogenization method with adaptive finite element methods, Comput. Meth. Appl. Mech. Eng. 83 (2) (1990) 143–198.

[23] O. Sigmund, S. Torquato, Design of materials with extreme thermal expansion using a three-phase topology optimization method, J. Mech. Phys. Solid 45 (6) (1997) 1037–1067.

[24] M. Montemurro, A. Catapano, D. Doroszewski, A multi-scale approach for the simultaneous shape and material optimisation of sandwich panels with cellular core, Compos. B. Eng. 91 (2016) 458–472.

[25] O. Sigmund, On the design of compliant mechanisms using topology optimization, Mech. Struct. Mach. 25 (4) (1997) 493–524.

[26] G. Allaire, Numerical Analysis and Optimization: An Introduction to Mathematical Modelling and Numerical Simulation, Oxford University Press, 2007.

[27] K. Svanberg, The method of moving asymptotes- a new method for structural optimization, Int. J. Numer. Meth. Eng. 24 (2) (1987) 359–373.

[28] A. Takezawa, S. Nishiwaki, M. Kitamura, Shape and topology optimization based on the phasefield method and sensitivity analysis, J. Comput. Phys. 229 (7) (2010) 2697–2718.

[29] Stratasys ltd. website. (accessed 9 april 2017).
URL http://www.stratasys.com/materials/material-safety-data-sheets/polyjet

[30] L. L. Howell, Compliant Mechanisms, Wiley-Interscience, New York, 2001.

[31] N. Lobontiu, Compliant Mechanisms: Design of Flexure Hinges, CRC Press, Florida, 2002.

[32] W. E. Frazier, Metal additive manufacturing: A review, J. Mater. Eng. Perform. 23 (6) (2014) 1917–1928.

[33] Q. Yang, P. Zhang, L. Cheng, Z. Min, M. Chyu, A. C. To, Finite element modeling and validation of thermomechanical behavior of ti-6al-4v in directed energy deposition additive manufacturing, Addit. Manuf. 12 (2016) 169–177.

[34] G. D. Janaki Ram, C. Robinson, Y. Yang, B. E. Stucker, Use of ultrasonic consolidation for fabrication of multi-material structures, Rapid Prototyping J. 13 (4) (2007) 226–235.

[35] D. Bourell, B. Stucker, J. O. Obielodan, A. Ceylan, L. E. Murr, B. E. Stucker, Multi-material bonding in ultrasonic consolidation, Rapid Prototyping J. 16 (3) (2010) 180–188.